Available online at www.sciencedirect.com
ScienceDirect
Journal of Power Sources 160 (2006) 18–26
JOURNAL OF POWER SOURCES
www.elsevier.com/locate/jpowsour

Mass/electron co-transports in an air-breathing cathode of a PEM fuel cell

J.J. Hwang [a,*], S.D. Wu [a], R.G. Pen [a], P.Y. Chen [a], C.H. Chao [b]

[a] *Research Center for Advanced Science and Technology, Mingdao University, Changhua 52345, Taiwan*
[b] *Department of Electrical Engineering, Ta-Hua Institute of Technology, Hsinchu County 307, Taiwan*

Received 16 September 2005; received in revised form 21 December 2005; accepted 4 January 2006
Available online 21 February 2006

Abstract

Mass/electron transports in a passive cathode of a proton exchange membrane (PEM) fuel cell have been studied numerically. The porous cathode in contact with a perforated current collector breathes fresh air through an array of orifices. Diffusions of reactant species in the porous cathodes are described by the Stefan–Maxwell equation. Electrochemical reaction on the surfaces of the porous cathode is depicted via the Butler–Volmer equation. Gas flow in the air-breathing porous cathodes is governed by isotropic linear resistance model with constant porosity and permeability. The electron/ion transports in the catalyst/electrolyte are dealt with the charge conservations based on the Ohm's law. A finite-element method is employed to solve the above-coupled equations. The effect of overpotential on the fluid flow, mass transport and electrochemistry is examined. Detailed electrochemical/mass characteristics such as flow velocities, species mass fraction, species flux and current density distributions are presented. They can provide a solid basis for optimizing the geometry of the PEM fuel cell stack running with a passive mode.

Keywords: Proton exchange membrane fuel cell; Air-breathing cathode; Porous; Transports

1. Introduction

The increasing number of portable electronic devices on the market today such as laptop computers, cellular phones, PDAs, remote-controlled toys, is creating a demand for improved, more environmentally friendly technologies in energy storage and conversion. Small-scale fuel cells are regarded as a potential candidate in replacing batteries in portable applications [1,2]. However, up to the present time, fuel cells were still too complicated and expensive to meet the need because they required cooling, humidification and pressurization sub-systems in operation. In response, researchers and engineers are trying to develop passive fuel cells for portable power applications. One interesting approach is air-breathing fuel cells, i.e. the oxygen needed by the electrochemical reaction is taken directly from the surrounding air by diffusion and/or natural convection. The fuel cell running in a passive manner has the benefits of minimizing the number of power consumed auxiliary devices that enhances the system efficiency. However, the power density of cell itself is not as good as that running in an active mode due to poor transport mechanisms [3–13]. It is well known that the current production by electrochemical reaction is directly proportional to the local oxygen concentration in the fuel cell. Inadequate airflow cannot provide enough oxygen for the electrochemical reaction on the active surfaces. It results in heterogeneous current distribution in the electrode that reduces the performance of the fuel cell. Thus, one of the most challenges in the design of passive fuel cells is how to feed the electrode with reactants and remove the products from the electrode appropriately.

The objective of the present paper is to numerically study the transport phenomena in a passive mode cathode of a PEM fuel cell that operates without external forced flows. The porous cathode is attached to a perforated current collector. It breathes the fresh air through the perforations and routes out the electric current through its solid counterpart. A set of conservation equations of mass, momentum, species and charge is developed. The Darcy law describes the fluid flow characteristics in the porous cathode. The Stefan–Maxwell equations illustrate the multi-species diffusion in the porous cathode. The Butler–Volmer equation depicts the electrochemical reaction on the surfaces of

* Corresponding author. Tel.: +886 48876660x1500; fax: +886 422518272.
E-mail address: azaijj@mdu.edu.tw (J.J. Hwang).

0378-7753/$ – see front matter © 2006 Elsevier B.V. All rights reserved.
doi:10.1016/j.jpowsour.2006.01.033

Nomenclature

c_i	mole concentration of the species i (mol m^{-3}), $c_i = \left[\frac{\omega_i}{M_i}/\sum_j^N \frac{\omega_j}{M_j}\right]\frac{P}{RT}$
D_{H_2O}	diffusivity of water vapor (m^2 s^{-1})
D_{O_2}	diffusivity of oxygen (m^2 s^{-1})
F	Faraday's constant
i_{ct}	current density (A m^{-2})
M	molecular weight (kg mol^{-1})
n	mass flux (kg m^2 s^{-1})
p	pressure (Pa)
$p_{i,m}$	possibility of the electrolyte in the connection of the catalyst layer
$p_{i,s}$	possibility of the catalyst in the connection of the catalyst layer
R	universal gas constant (W mol^{-1} K^{-1})
T	temperature (K)
u	velocity vectors (m s^{-1})
x, y, z	coordinate system, Fig. 1 (m)

Greek symbols

α	symmetric factor
ε	cathode porosity
ϕ_l	potential of the ionic conductor (electrolyte-phase) (V)
ϕ_s	potential of the electric conductor (catalyst-phase) (V)
η_t	total overpotential across the computational module (V)
κ	permeability (m^2)
μ	dynamic viscosity (m s^{-2})
ρ	density (kg m^3)
σ_l	ionic conductivity of the membrane phase (S m^{-1})
σ_s	electric conductivity of the catalyst-phase (S m^{-1})
τ	tortuosity
υ_l	volume fraction of the ionic conductor (electrolyte-phase) in the cathode
υ_s	volume fraction of the electronic conductor (catalyst-phase) in the cathode
ω	mass fraction

the porous cathode. A finite-element based computational fluid dynamics (CFD) [14,15] methodology is employed to solve the multi-physics transports in the air-breathing cathode of a PEM fuel cell. Emphasis is placed on the effect of the total overpotential on the species/electron co-transports in a porous cathode of a PEM fuel cell. The relation between the current distributions and the mass transports are discussed in detail. The informative results obtained by the present study can help in understanding of the local gas transports and electrochemical characteristics in an air-breathing PEM fuel cell. Also, they can provide a solid basis for optimizing the geometry of the passive PEM fuel cell stack.

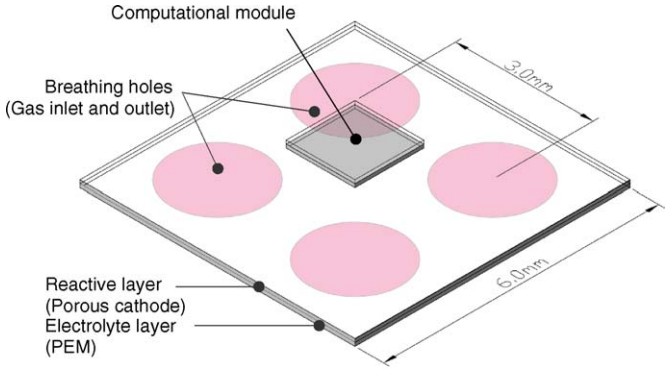

Fig. 1. Fuel cell cathode with a perforated current collector.

2. Model descriptions

2.1. Governing equations

Fig. 1 shows a typical geometry of a self-breathing cathode of a PEM fuel cell with perforated current collectors, which is often seen in mini- or micro-fuel cells [16,17]. The pink circular zones on top surfaces of the module are the cathode inlets that are open to the ambient, while the rest of the top surfaces sit flush against the current collector. Due to the perforation layout, a 3D model is needed to simulate the mass transport, current and reaction distributions. For memory and time saving, a unit cell shown in Fig. 2 is considered in the present study. The unit cell is 1.5 mm × 1.5 mm in surface, and the gas inlet/outlet hole has a radius of 1.0 mm. Both the reactive layer and the electrolyte layer are 75 μm thick. The origin of the coordinate system is set to the remote corner of the unit cell, as shown in Fig. 2.

The upper rectangular domain is a porous structure that contains the feed gas mixture, an electronically conducting material (catalyst) and an ionically conducting material (electrolyte). The oxygen reduction reaction takes place in the reactive layer. It can be represented by the following equations.

$$O_2 + 4H^+ + 4e^- \rightarrow 2H_2O \quad (1)$$

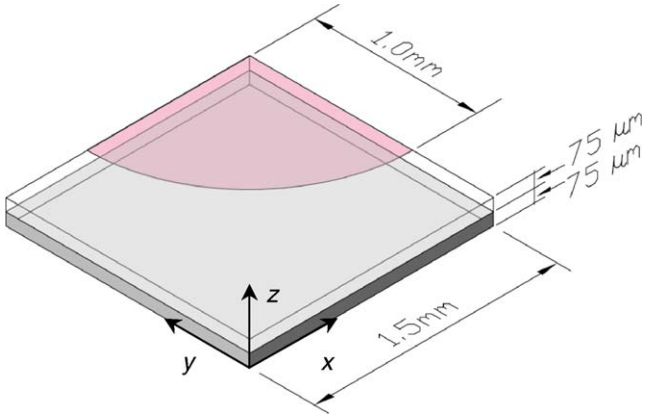

Fig. 2. Dimensions and the coordinate system of the computational module.

Note that the circular holes in the collector are not only the entrance of the fresh air but also the exit of the products (water vapor) of the electrochemical reaction.

The lower domain corresponds to an electrolyte layer (PEM), interconnecting the two electrodes of the fuel cell. No reaction takes place in this layer. Neither are there pores to allow gas to flow nor material for electronic current. The ionic current balance in the electrolyte membrane between the anode and the cathode is given by:

$$\nabla(-\sigma_{\mathrm{l}}\,\nabla\phi_{\mathrm{l}}) = 0 \tag{2}$$

where σ_1 is the ionic conductivity of the electrolyte and ϕ_{l} is the electrolyte potential.

Two kinds of solid materials consist of the porous matrices of the cathode i.e., electrolyte (ionic conductor) and catalyst (electronic conductor). A potential difference exists between the electrolyte and the catalyst to drive the transfer current, keeping the electrochemical reaction continuously. The current passes through cathode can be decomposed two parts, i.e.,

$$i = i_{\mathrm{s}} + i_{\mathrm{l}} \tag{3}$$

i_{s} and i_{l} are the currents flowing through the catalyst and the electrolyte, respectively. Since the cathodes are electroneutral everywhere, there is no charge-buildup in the catalyst layers. Thus, the charge conservation is

$$\nabla \cdot i = 0 \tag{4}$$

That is

$$\nabla \cdot i_{\mathrm{s}} = -\nabla \cdot i_{\mathrm{l}} \tag{5}$$

These two current components interact through electrochemical reactions. The electrons are transferred to the electrolyte from the catalyst. Application of Ohm's law to equation yields the current conservation:

$$\nabla \cdot (-\sigma_{\mathrm{s,eff}}\,\nabla\phi_{\mathrm{s}}) = \; -S_{\mathrm{a}} \cdot i_{\mathrm{ct}} \tag{6}$$

$$\nabla \cdot (-\sigma_{\mathrm{l,eff}}\,\nabla\phi_{\mathrm{l}}) = S_{\mathrm{a}} \cdot i_{\mathrm{ct}} \tag{7}$$

where ϕ_{s} and ϕ_{l} are the catalyst potential and the electrolyte potential, respectively. S_{a} is the surface area-to-volume ratio, and i_{ct} is the local transfer current density. $\sigma_{\mathrm{s,eff}}$ and $\sigma_{\mathrm{1,eff}}$ are the effective electronic and ionic conductivities of the catalyst and electrolyte, respectively. They are modeled as

$$\sigma_{\mathrm{s,eff}} = \sigma_{\mathrm{s}}(1-\varepsilon_{\mathrm{c}}) \times \upsilon_{\mathrm{s}} \times p_{i,\mathrm{s}} \tag{8}$$

$$\sigma_{\mathrm{l,eff}} = \sigma_{\mathrm{l}}(1-\varepsilon_{\mathrm{c}}) \times \upsilon_{\mathrm{l}} \times p_{i,\mathrm{l}} \tag{9}$$

where υ_{s} and υ_{l} are the volume fraction of the catalyst and electrolyte in the catalyst layer, respectively. $p_{i,\mathrm{s}}$ and $p_{i,\mathrm{l}}$ are the possibilities of the catalyst and electrolyte in the connection of the catalyst layer, respectively [18,19]. It is noted that only a long-range connection of the same particles stretch from the catalyst layer to the electrolyte ensures good conductivity.

The conservations of species for oxygen, water vapor and nitrogen in the gas phase are, respectively, expressed as

$$\nabla \cdot (\rho\mathbf{u}\omega_{\mathrm{O_2}}) = \rho D_{\mathrm{O_2,\,eff}}\,\nabla\omega_{\mathrm{O_2}} + \frac{\rho\omega_{\mathrm{O_2}}}{M} D_{\mathrm{O_2}}\,\nabla M + S_{\mathrm{O_2}} \tag{10}$$

$$\nabla \cdot (\rho\mathbf{u}\omega_{\mathrm{H_2O}}) = \rho D_{\mathrm{H_2O,eff}}\,\nabla\omega_{\mathrm{O_2}} + \frac{\rho\omega_{\mathrm{O_2}}}{M} D_{\mathrm{H_2O}}\,\nabla M + S_{\mathrm{H_2O}} \tag{11}$$

$$\omega_{\mathrm{N_2}} = 1 - \omega_{\mathrm{O_2}} - \omega_{\mathrm{H_2O}} \tag{12}$$

where ρ is the density of the gas mixture, $\mathbf{u}$ the velocity vector and M is the mole masses of the mixture,. The first term on the right-hand side of Eqs. (10) and (11) represents the Fickian diffusion due to concentration gradient. While the second one on the right-hand side of Eqs. (10) and (11) is the correction to enforce the Stefan–Maxwell equations for the multi-component diffusion system. The source terms of the mass balances for oxygen and water vapor are, respectively, given by:

$$S_{\mathrm{O_2}} = -\frac{i_{\mathrm{ct}} S_{\mathrm{a}} M_{\mathrm{O_2}}}{4F} \tag{13}$$

$$S_{\mathrm{H_2O}} = \frac{i_{\mathrm{ct}} S_{\mathrm{a}} M_{\mathrm{H_2O}}}{2F} \tag{14}$$

where F is the Faraday's constant. The above effective diffusivities follow the Bruggemann model [13] that describes the species diffuses in the porous electrode of a multi-component mixture system, i.e.,

$$D_{\mathrm{O_2,eff}} = \varepsilon^{\tau} D_{\mathrm{O_2}} \tag{15}$$

$$D_{\mathrm{H_2O,eff}} = \varepsilon^{\tau} D_{\mathrm{H_2O}} \tag{16}$$

The velocity vector is coupled to Darcy's law accordingly:

$$\mathbf{u} = -\frac{\kappa}{\mu}\,\nabla p \tag{17}$$

where κ is the permeability, μ the viscosity and p is the pressure. The continuity equation for the gas flow mixture is the sum of the continuity for the three involved species, which yields:

$$\nabla\left(\rho\frac{\kappa}{\mu}\,\nabla p\right) = \frac{i_{\mathrm{ct}} S_{\mathrm{a}} M}{4F} - \frac{i_{\mathrm{ct}} S_{\mathrm{a}} M_{\mathrm{H_2O}}}{2F} \tag{18}$$

The local charge transfer current density couples the current balances with the mass balances, according to:

$$i_{\mathrm{ct}} = i_{\mathrm{o}}\left\{\left(\frac{c_{\mathrm{O_2}}}{c_{\mathrm{O_2,ref}}}\right)\exp\left[\frac{4\alpha F}{RT}(\phi_{\mathrm{l}}-\phi_{\mathrm{s}})\right] - \left(\frac{c_{\mathrm{H_2O}}}{c_{\mathrm{H_2O,ref}}}\right)^{2}\exp\left[\frac{4(1-\alpha)F}{RT}(\phi_{\mathrm{l}}-\phi_{\mathrm{s}})\right]\right\} \tag{19}$$

where α is the symmetric factor, R the universal gas constant and T is the temperature. $c_{\mathrm{O_2}}$ and $c_{\mathrm{H_2O}}$ are the concentrations of oxygen and water vapor, respectively.

2.2. Boundary conditions

The boundary conditions for the ionic current balances are insulating at all boundaries, i.e.,

$$n \cdot (-\sigma_{\mathrm{l,eff}}\,\nabla\phi_{\mathrm{l}}) = 0 \tag{20}$$

except for the lowest boundary for the electrolyte layer. The condition at this boundary sets the ionic potential:

$$\phi_l = \phi_{l,0} \tag{21}$$

The boundaries for the electronic current balance are those that encompass the cathode sub-domain. The boundary conditions are all insulating except for the current collector boundary where the potential is set to zero (ground connection):

$$\phi_s = 0 \tag{22}$$

The boundary conditions for the species balances are also those that encompass the electrode sub-domain and are all insulating except for the gas channel boundary. The conditions at the module inlet (perforations) are given by the composition of the inlet gas

$$\omega_i = \omega_{i,0} \tag{23}$$

For the momentum balance through Darcy's law, all boundaries are insulating:

$$n \cdot \left(\frac{\kappa}{\mu} \nabla p \right) = 0 \tag{24}$$

except for the module inlet, where the pressure is set:

$$p = p_{atm} \tag{25}$$

The input data to the model is given in Table 1.

2.3. Numerical schemes

The governing equations are numerically solved by the finite-element method [20–22]. It uses the Broyden's method with an LU-decomposition pre-conditioner to solve the non-linear equations iteratively. To reduce continuity errors, a penalty term is employed for pressure. Thus, there is a continuous part of the pressure and piecewise constant part providing and extra degree of freedom (DOF) for pressure on each element. It uses Newton–Raphson iteration to solve the close-coupled groups (velocity, pressure, temperature, concentration and electricity) and uses the frontal algorithm (Gaussian elimination) to solve the linearized system of equations for each iteration.

In the computational domain, a total of 1828 nodes and 8789 meshes were used (quadratic velocities in each direction). Additional runs for the coarser meshes, 7712, and the finer meshes, 10982, are taken for a check of grid independence. The program gives results within 1% of each other on the finest meshes used. A comparison of the results of the two mesh sizes, 8789 and 10982, shows that the maximum discrepancies in the axial velocity and oxygen concentration profiles are 1.5 and 1.6%, respectively. In addition, results indicate a maximum change of 2.1% in current density distribution between the solutions of 8789 and 10982 meshes. These changes are so small that the accuracy of the solutions on 8789 meshes is deemed satisfactory. Solutions are considered to be converged at each test condition after the ratio of residual source (including mass, momentum and species) to the maximum flux across a control surface becomes below $1.0 \times 10^{-}6$. The CPU time ranged from 100 to 500 min

Table 1
Electrochemical and flow characteristic data used in the present model

Expression	Symbols	Data
Exchange current density (A m^2)	i_o	1.0×10^{-3}
Surface to volume ratio (m^{-1})	S_a	1.0×10^9
Ambient temperature (K)	T	353
Electric conductivity of the catalyst (S m^{-1})	σ_s	1000
Ionic conductivity of the electrolyte (S m^{-1})	σ_1	5.0[1]
Dynamic viscosity of gas mixture (m s^{-2})	μ	3.0×10^{-5}
Porosity of the cathode	ε	0.4
Permeability of the cathode (m^2)	κ	1.0×10^{-9}
Reference mole fraction of oxygen	$c_{O_2,ref}$	3.6641
Reference mole fraction of water	$c_{O_2,ref}$	3.6641
Ambient pressure (Pa)	p_{in}	1.013×10^5
N_2 molecular weight (kg mol^{-1})	M_{N_2}	0.028
O_2 molecular weight (kg mol^{-1})	M_{O_2}	0.032[1]
H_2O molecular weight (kg mol^{-1})	M_{H_2O}	0.018
Mass fraction of O_2 at inlet	$\omega_{O_2,in}$	0.233
Mass fraction of N_2 at inlet	$\omega_{N_2,in}$	0.766
Mass fraction of H_2O at inlet	$\omega_{H_2O,in}$	0.001

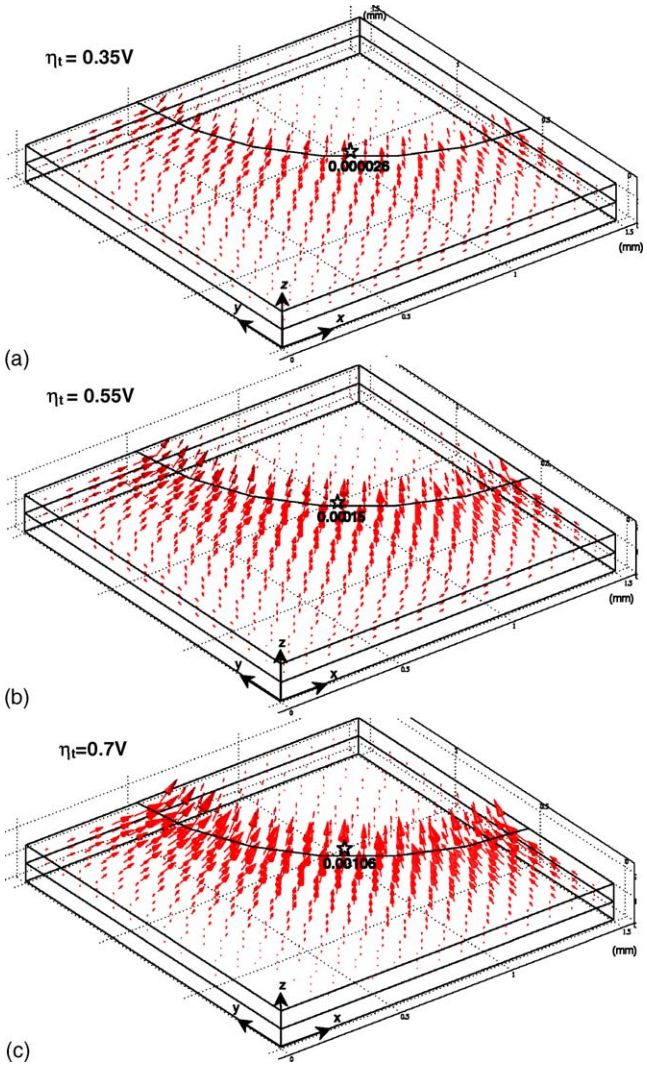

Fig. 3. Effect of overpotential on the velocity distributions: (a) $\eta_t = 0.35$ V, (b) $\eta_t = 0.55$V and (c) $\eta_t = 0.70$ V (unit: m s^{-1}).

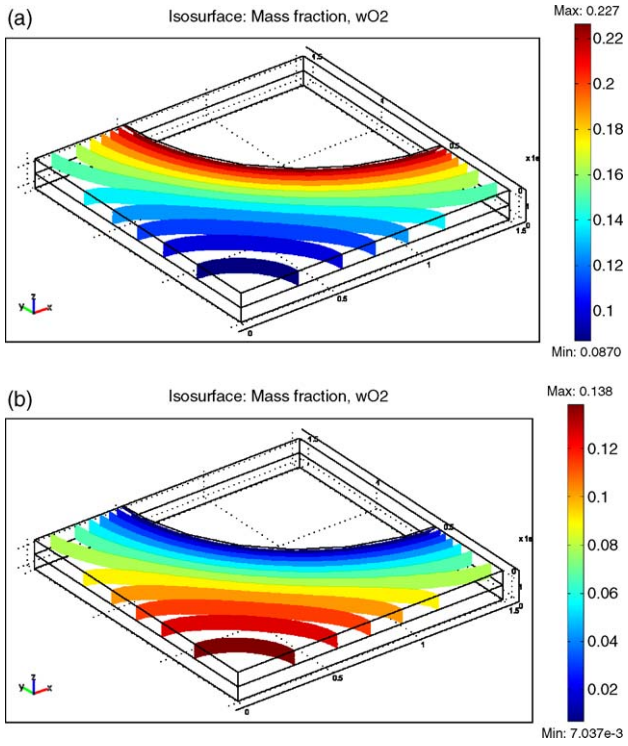

Fig. 4. Iso-surface distributions of oxygen mass fractions and water vapor mass fractions, $\eta_t = 0.55$ V.

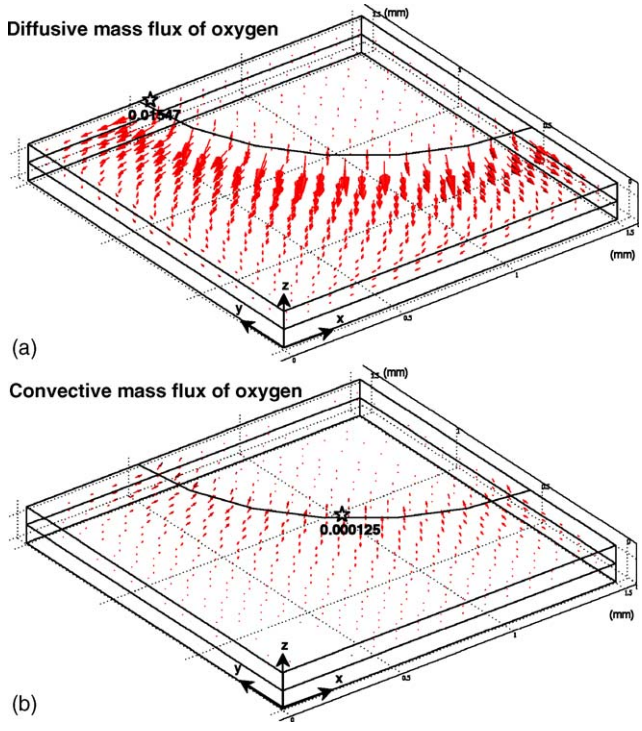

Fig. 5. Comparison of (a) diffusive oxygen mass flux and (b) convective oxygen mass flux at, $\eta_t = 0.55$ V (kg m^{-2} s^{-1}).

on a Pentium IV PC (2.8 GHz, 2 GB RAM) using Windows XP operating system.

3. Results and discussion

Fig. 3 shows the effect of overpotential on the gas velocity distributions in the porous cathode. Clearly, the vectors direct the gas flow from the interface of the PEM and the cathode toward to the orifice. In addition, a higher overpotential with a stronger electrochemical reaction has larger outward flow velocities in the cathode. The outward flow seems be contrary to the common sense that the fresh air should flow into the cathode from the ambient. Such transport phenomena are illustrated as follows. In the present geometric design, the orifice acts as not only an inlet of the reactants (O_2) but also an outlet of the products (H_2O). The oxygen diffuses into the porous cathode through the orifices and then is consumed continuously for keeping the oxygen reduction reaction (Eq. (1)). Actually, the oxygen reduction reaction will increase the bulk mass of the gas mixture by producing the water vapor. Thus, the gas mixture should flow outward to satisfy the continuity. It is further seen from these figures that significant

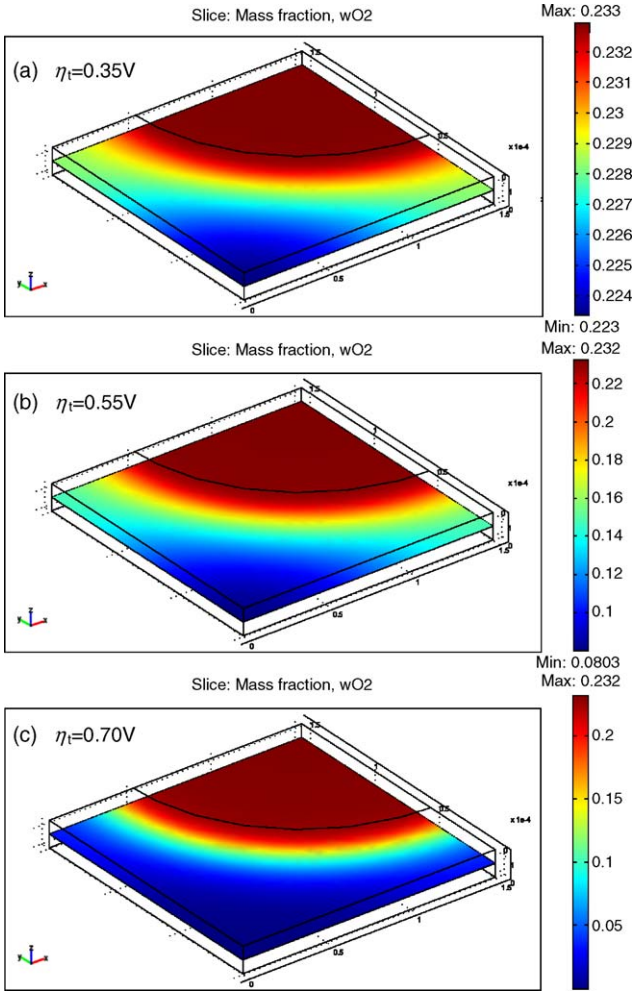

Fig. 6. Effect of the total overpotential on the mass fraction distributions on the interface of electrolyte membrane and catalyst layer ($z = 0.000075$ mm). (a) $\eta_t = 0.35$ V, (b) 0.55 V and (c) 0.70 V.

velocity peaks occur around the edge of the orifice, as denoted by star symbols in each plot. This is a contribution of the products (water vapor) in the reactive layer beneath the current collector.

Fig. 4(a and b) show the iso-surfaces of the oxygen mass fraction (ω_{O_2}) and the water vapor mass fraction (ω_{H_2O}) in the porous cathode, respectively. The oxygen mass fraction in the porous cathode under the orifice is almost constant. It decreases from the orifice to the remote corner of the domain, i.e., $x=0$, $y=0$. In contrast, the water vapor mass fraction has an inverse trend that the remote corner has higher values of ω_{H_2O} and the orifice has lower values of ω_{H_2O}. In addition, both the oxygen mass fraction and the water vapor mass fraction seem to be unaltered along the z-direction.

Two kinds of mass fluxes in the porous cathode can be decomposed from the total oxygen mass fluxes, i.e., diffusive mass flux and convective mass flux. As shown in Fig. 5(a), the oxygen diffusive flux directs inward, which is driven by the oxygen concentration gradient. In contrast, the oxygen convective flux directs outward that follows the gas flow direction that shows in Fig. 3. It is seen that the magnitude of the diffusive flux is significantly larger than that of the convective flux. Form the integrated results of the quarter of the orifice the diffusive mass flux for the oxygen is about 300 times of convective one. Therefore, the diffusion dominates the mass transports in the air-breathing cathode.

Fig. 6(a–c) show the distributions of the oxygen mass fraction (ω_{O_2}) at the interface between the PEM and the cathode for three different total overpotentials, i.e., $\eta_t = 0.35$, 0.55 and 0.7 V, respectively. It is seen from these figures that the projective area from the orifice has a high oxygen mass fraction. It decreases as the oxygen gradually diffuses into the cathode beneath the current collector. The remote corner ($x=0$, $y=0$) has a local minimum mass fraction for oxygen since it has the longest distance from the orifice and thus cannot sense the fresh air easily. In general, the oxygen mass fraction decreases with increasing the total overpotential. At the highest total overpotential (Fig. 6(c)), the oxygen is depleted almost.

Fig. 7(a and b) display several slices cutting across the x and y planes showing the distributions of the electrolyte-phase potential (ϕ_l) and the catalyst-phase potential (ϕ_s) in the computational module, respectively. No data of catalyst potential are shown in the electrolyte layer, since it is free of the catalyst. It is seen in Fig. 7(a), the potential of the electrolyte-phase has the highest value on the bottom surface of the module ($z=0$). It decreases along the z-direction due to the ohmic resistance. In addition, a significant drop of the electrolyte-phase potential is found near the orifice edge. It is because a large amount of ionic current should traverse here to transfer the current to the catalyst-phase through the electrochemical reaction. As for the potential catalyst-phase (Fig. 7(b)), the region under the current

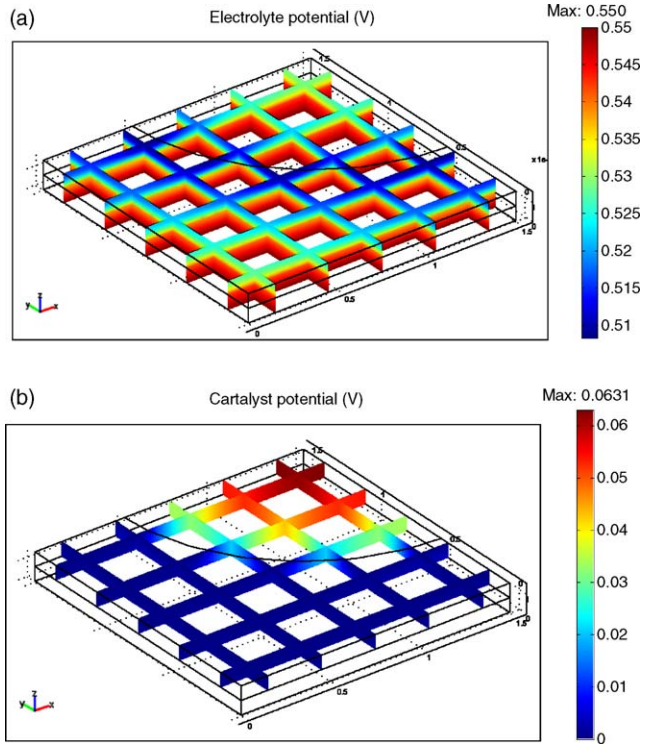

Fig. 7. Comparison of electrolyte potential and catalyst potential, (a) electrolyte potential (ϕ_l) and (b) catalyst potential (ϕ_s) (unit: V).

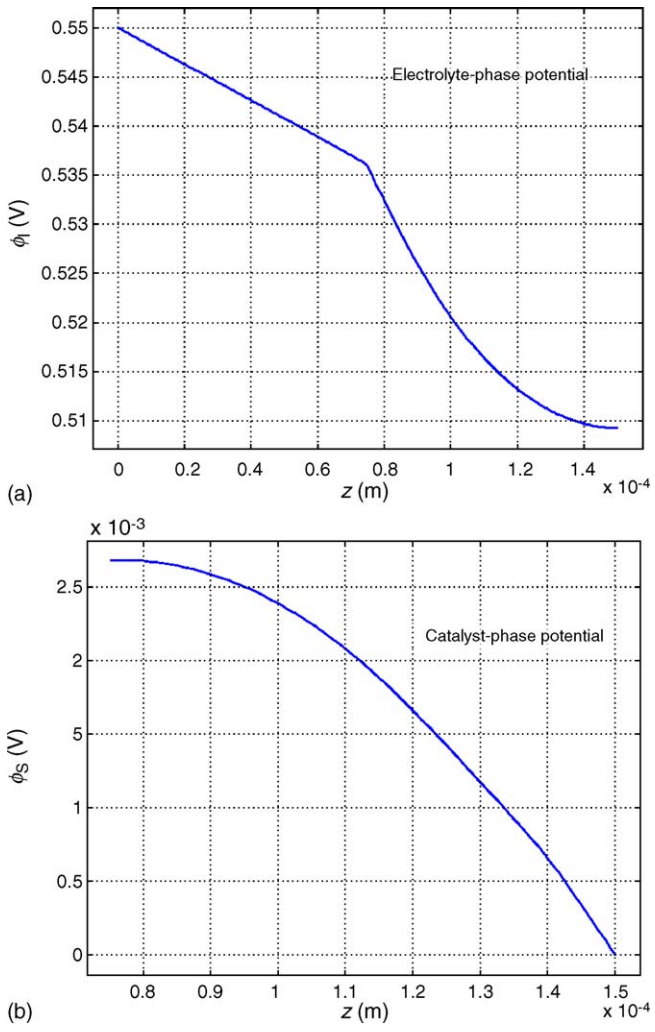

Fig. 8. Potential distributions along thickness direction (z) at $x=0.75$ mm and $y=0.75$ mm: (a) electrolyte-phase and (b) catalyst-phase.

collector has null potential almost, meaning that the porous cathode well connects to the current collector and the ohmic resistance is negligible almost. In addition, a longer distance of through-flow current from the region under the orifice to the current collector requires a higher electric potential.

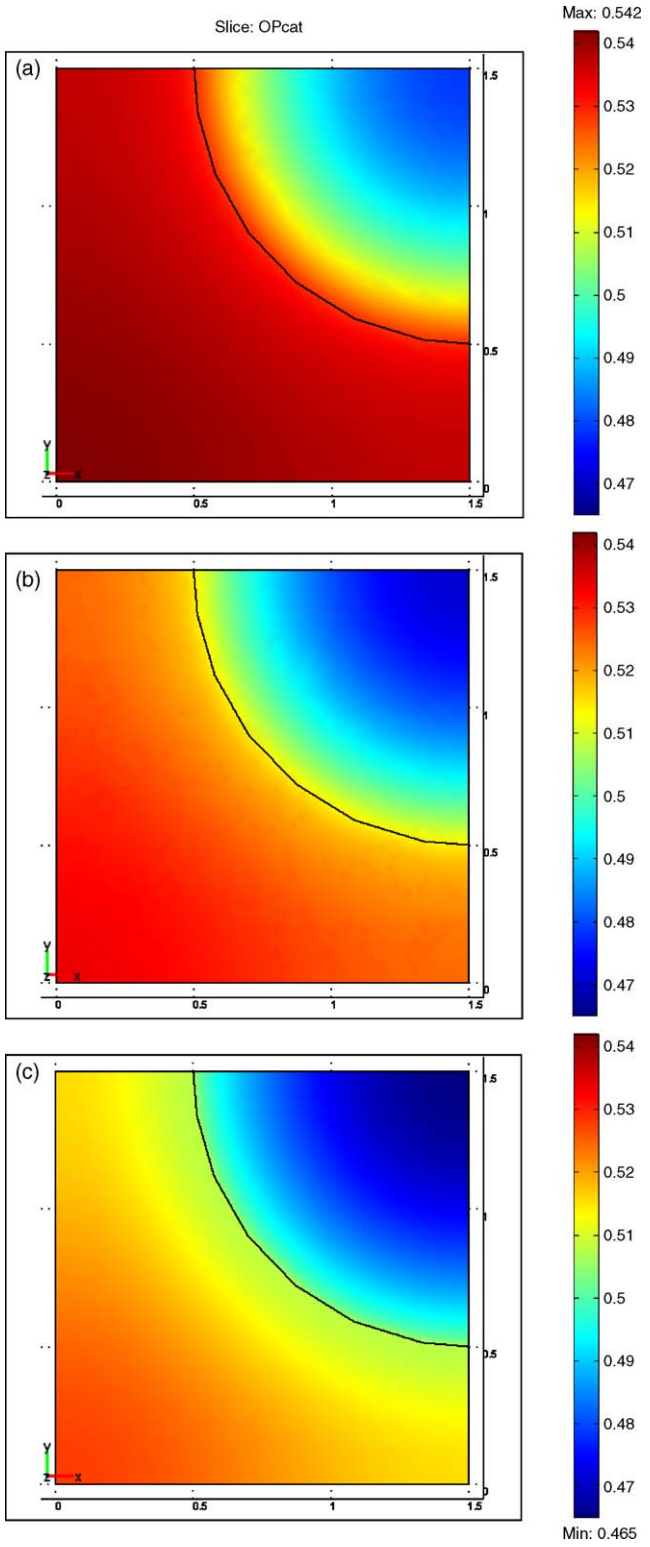

Fig. 9. Overpotential ($\phi_l - \phi_s$) distributions at three elevations: (a) $z = 0.075$ mm, (b) $z = 0.1$ mm and (c) $z = 0.15$ mm (unit: V).

Fig. 8 shows the potential distributions along the z-direction at the module middle ($x = 0.750$ mm, $y = 0.75$ mm). Focus is first placed on the distribution of the electrolyte-phase potential (Fig. 8(a)). A linear drop of the electrolyte-phase potential between $z = 0$ and 0.75 mm reflects a constant ohmic resistance in the PEM. In the porous cathode, 0.75 mm $\times$ z $\times$ 1.5 mm, the electrolyte-phase potential drops sharply first and then declines mildly. The sharp drop of ϕ_l is because the through-flow area for the ionic current is reduced when it enters the porous cathode from the PEM. As the ionic current moves forward to the current collector ($z = 0.15$ mm), the ionic current transfers itself gradually to the catalyst by the electrochemical reaction and thus eases off the drop of the electrolyte-phase potential. In a similar transport manner, the potential distribution of the catalyst-phase starts with a mild decline and then drops significantly to zero at the interface with the current collector.

In the porous cathode, the difference between the electrolyte-phase potential and the catalyst-phase potential, $\phi_l - \phi_s$, represents the cathodic overpotential, including the activation overpotential and the concentration overpotential. Fig. 9 depicts the local cathodic overpotential distributions on three selected elevations of the porous cathode, i.e., $z = 0.075$, 0.1 and 0.15 mm, respectively. It is seen that the local cathodic overpotentials are rather even in throughout the cathode. At a fixed elevation, the cathodic overpotential in the region beneath the orifice is significant. In addition, the cathodic overpotential is higher near the PEM than near the current collector. It is because the oxygen concentration is lower and electrochemical reaction that requires a larger overpotential to drive the transfer current between the electrolyte and the catalyst.

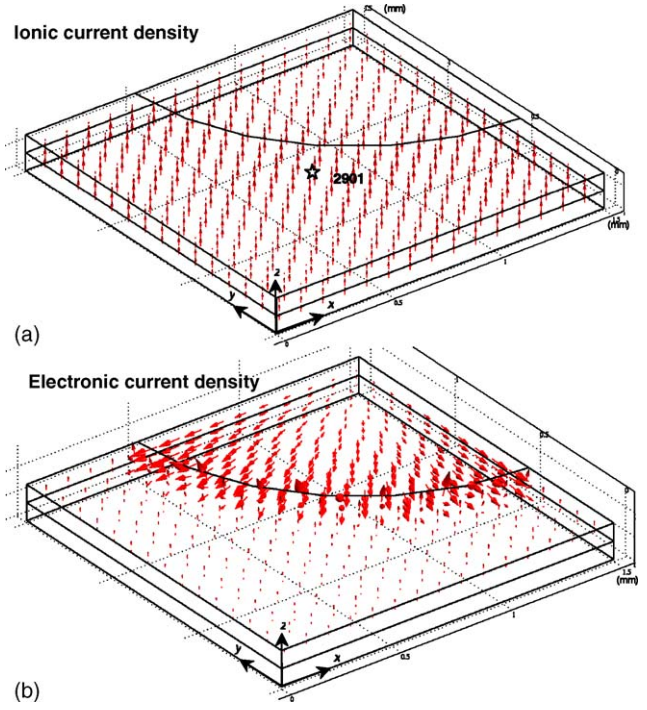

Fig. 10. Ionic current density distributions and electronic current density distributions (unit: A cm^{-2}).

The electrochemical reaction rate, represented by the local current density, is related to both the local overpotential and the oxygen concentration. Fig. 10(a and b) show the vector distributions of the ionic current density and the electronic current density in the computational module, respectively. The ionic current directs monotonously from the bottom to the top of the module. In contrast, the electronic current density distribution shows a large variation. It directs toward the current collector from everywhere of the cathode. Again, the current production by the electrochemical reaction is higher beneath the orifice that causes a high current density in the region around the edge of the orifice.

Fig. 11 shows the distributions of the ionic current density and the electronic current density along the z-direction at the middle of the computational module ($x = 0.75$ mm, $y = 0.75$ mm). As shown in Fig. 11(a), the ionic current density does not alter in the PEM but drops significantly in the porous cathode. The extent of the current density drop represents the degree of the electrochemical reaction. It becomes zero at the interface with the current collector. As for the electronic current density, it traverses through the catalyst in the porous cathode, and increases downstream due to the current accumulation that is transferred from the electrolyte.

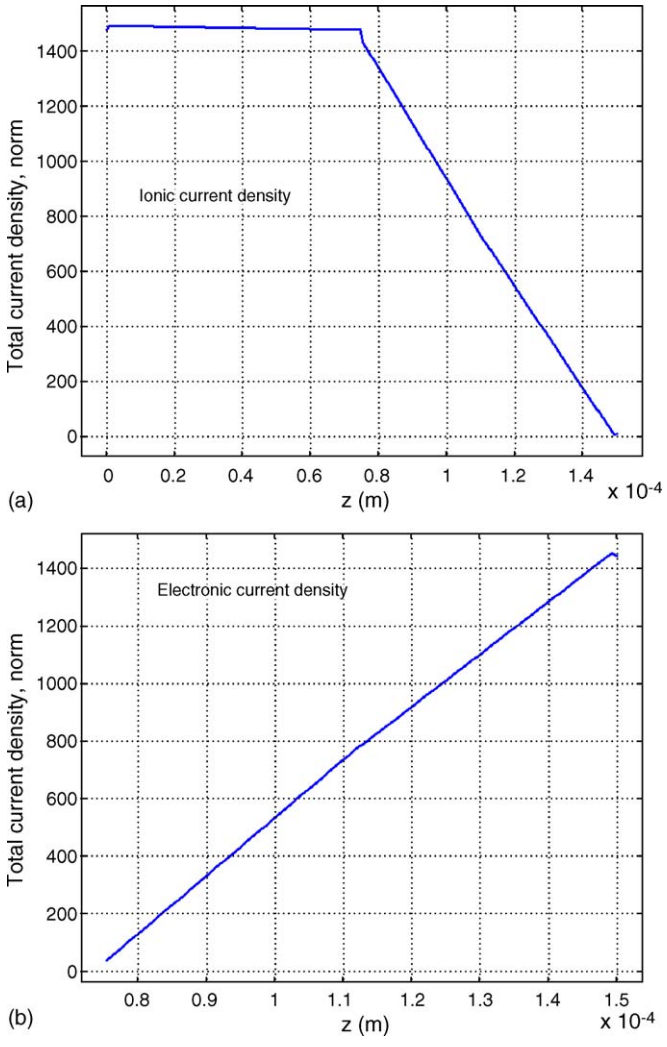

Fig. 11. Current density distributions along the z direction at $x = 0$, $y = 0$: (a) ionic current density and (b) electronic current density (unit: A m^{-2}).

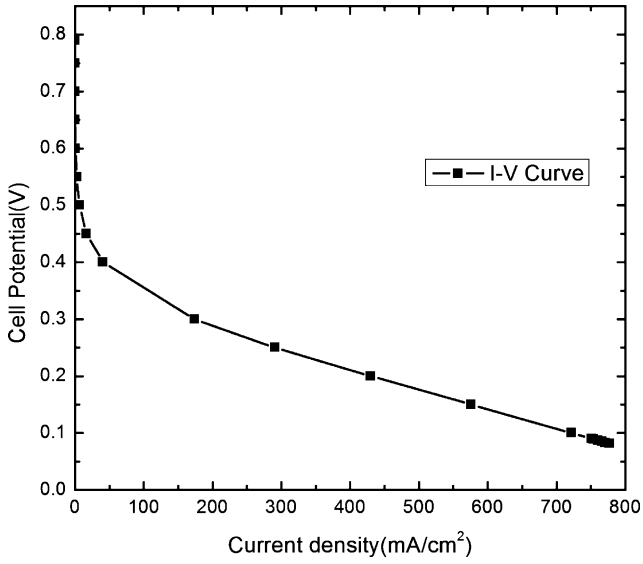

Fig. 12. Polarization curve of the air-breathing cathode.

Fig. 12 shows the polarization curve of the present air-breathing cathode. The data shown in the vertical coordinate is represented by the value that subtracts the total overpotential from the open circuit voltage of the fuel cell. If the anodic overpotential is negligible, the above data can stand well for the cell potential, V_{cell}. It is seen that cell potential drops significantly at the lower current density and decreases mildly as the current density increases, which is typical of the PEM fuel cell.

4. Concluding remarks

A three-dimensional model of coupled fluid flow field, mass transport and electrochemistry in an air-breathing cathode of a PEM fuel cell is presented. Conservative equations describing the co-transports of mass, momentum, species and charge are developed. A finite-element based CFD method is employed to solve the above-coupled equations with proper account of electrochemical kinetics. The model has implemented a voltage-to-current algorithm, coupling of the potential field with the species concentration field. A realistic spatial variation of electrochemical kinetics is thus obtained by simultaneously solving the electron transport equations of the catalyst and electrolyte in the porous cathode. The effect of the total overpotential on the distributions of reactant gas mass fraction, overpotential and current density in the porous cathode are presented and discussed in detail. They can help in understanding of the gas-transport mechanisms and electrochemical characteristics in an air-breathing PEM fuel cell, and thus provide a solid base for optimizing the geometry of the passive PEM fuel cell stack.

Acknowledgment

This research was partly sponsored by the National Science Council of Taiwan under contract no. NSC 93-2212-E-451-002.

References

[1] C.K. Dyer, J. Power Sources 106 (2002) 31–34.
[2] A. Heinzel, C. Hebling, M. Müuller, M. Zedda, C. Müller, J. Power Sources 105 (2002) 250–255.
[3] D. Chu, R. Jiang, J. Power Sources 83 (1999) 128–133.
[4] S. Morner, S.A. Klein, J. Sol. Energy Eng. 123 (2001) 225–231.
[5] M. Noponen, T. Mennola, M. Mikkola, T. Hottinen, P. Lund, J. Power Sources 106 (2002) 304–312.
[6] M. Noponen, T. Hottinen, T. Mennola, M. Mikkola, P. Lund, J. Appl. Electrochem. 32 (2002) 1081–1089.
[7] T. Mennola, M. Mikkola, M. Noponen, T. Hottinen, P. Lund, J. Power Sources 112 (2002) 261–272.
[8] P.W. Li, T. Zhang, Q.M. Wang, L. Schaefer, M.K. Chyu, J. Power Sources 114 (2003) 63–69.
[9] T. Hottinen, M. Noponen, T. Mennola, O. Himanen, M. Mikkola, P. Lund, J. Appl. Electrochem. 33 (2003) 265–271.
[10] A. Schmitz, M. Tranitz, S. Wagner, R. Hahn, C. Hebling, J. Power Sources 118 (2003) 162–171.
[11] T. Mennola, M. Noponen, T. Kallio, M. Mikkola, T. Hottinen, J. Appl. Electrochem. 34 (2004) 31–36.
[12] A. Schmitz, S. Wagner, R. Hahn, H. Uzun, C. Hebling, J. Power Sources 127 (2004) 197–205.
[13] T. Hottinen, M. Mikkola, P. Lund, J. Power Sources 129 (2004) 68–72.
[14] J.J. Hwang, C.K. Chen, D.Y. Lai, J. Power Sources 140 (2005) 235–242.
[15] J.J. Hwang, D.Y. Lai, C.K. Chen, J. Power Sources 143 (2005) 75–83.
[16] J.M. Moore, J.B. Lakeman, G.O. Mepsted, J. Power Sources 106 (2002) 16–20.
[17] F. Jaouena, S. Haasl, W. Wijngaart, A. Lundblada, G. Lindbergh, G. Stemme, J. Power Sources 144 (2005) 113–121.
[18] J.J. Hwang, J. ASME, Fuel Cell Sci. Technol. 2 (2005) 164–170.
[19] C.H. Kuo, P.K. Gupta, Acta Metall. Matter 39 (1995) 397.
[20] J.J. Hwang, J. Electrochem. Soc. 153 (2006) A216.